RSC Advances

PAPER

View Article Online
View Journal | View Issue

Cite this: *RSC Adv.*, 2025, **15**, 32871

Glycosylated 18β-glycyrrhetinic acid derivatives as promising inhibitors of the SARS-CoV-2 main protease

En-You Liao,[a] Shen-Chieh Chou,[a] Tzu-Yu Huang,[a] Sheng-Cih Huang,[a] Teng-Kai Yu,[a] Feng-Pai Chou*[ab] and Tung-Kung Wu *[abc]

Received 1st July 2025
Accepted 28th August 2025

DOI: 10.1039/d5ra04664e

rsc.li/rsc-advances

The SARS-CoV-2 main protease (M^{pro}) is a validated antiviral target for COVID-19 therapeutics due to its essential role in viral replication and absence of human homologs. Here, we report the synthesis and characterization of glycosylated 18β-glycyrrhetinic acid (18β-GA) derivatives using a one-pot, four-enzyme system to improve drug-like properties and antiviral efficacy. Among the derivatives, 18β-GA-3-*O*-β-Glc and 18β-GA-30-*O*-β-Glc exhibited promising M^{pro} inhibition, with IC_{50} values of 8.70 ± 0.80 μM and 4.77 ± 0.49 μM, respectively. Biolayer interferometry revealed favorable binding affinities and reversible interactions with M^{pro}, while molecular docking demonstrated their stable binding conformations resembling that of GC376. These glycosides also showed improved predicted oral bioavailability and physicochemical profiles. Our findings support the potential of glycosylated 18β-GA derivatives as cost-effective and scalable antiviral candidates targeting SARS-CoV-2 M^{pro}.

1. Introduction

The global outbreak of coronavirus disease 2019 (COVID-19), caused by the novel Severe Acute Respiratory Syndrome Coronavirus 2 (SARS-CoV-2), has had a profound impact on daily life, healthcare systems, and the global economy, resulting in significant social and financial losses. Although several antiviral drugs, such as remdesivir, Paxlovid, and molnupiravir have been approved for early-stage treatment, and vaccines have been developed to enhance immune protection, the endemic infection resurged in 2025 due to ongoing viral mutations.[1–4] COVID-19 remains particularly dangerous for the elderly, immunocompromised individuals, and patients with chronic conditions such as diabetes, cancer, and cardiovascular disease. Emerging SARS-CoV-2 Omicron variants, including NB.1.8.1 and XFG sub-variants, have diminished vaccine efficacy and contributed to sustained viral transmission. Although current antiviral therapies offer some clinical benefit, their use is limited by high cost, inconsistent effectiveness, drug resistance, and limited accessibility in low-resource settings.[5] These challenges highlight the urgent need for the development of novel antiviral agents that are affordable, orally available, and target conserved viral proteins.[6–8] Among several potential drug targets, such as the spike (S) protein, papain-like protease (PL^{pro}), RNA-dependent RNA polymerase (RdRP), and NTPase/helicase (nsp13), the main protease (M^{pro} or $3CL^{pro}$, nsp5) stands out as a particularly attractive antiviral target due to its essential role in viral replication and its unique substrate recognition sequence (Leu–Gln↓(Ser, Ala, Gly)), which is absent in human proteases. Inhibiting M^{pro} can effectively block viral replication without harming host cells.[9,10] However, many M^{pro} inhibitors have failed to reach clinical application due to suboptimal pharmacokinetics and limited therapeutic efficacy (ref. 11 and references therein). Nevertheless, the past success of M^{pro} inhibitors developed for SARS-CoV and MERS-CoV validates M^{pro} as a conserved and viable antiviral target. Continued efforts are needed to develop novel M^{pro} inhibitors with improved therapeutic profiles for more effective COVID-19 treatment.

Glycyrrhizin (GL, **1**), a major triterpenoid saponin isolated from licorice root, is composed of two glucuronic acid units and one glycyrrhetinic acid (GA). It has been shown to exhibit broad-spectrum antiviral activity against various viruses, including hepatitis A, B, and C, herpes simplex virus, human immunodeficiency virus type 1 (HIV-1), and SARS-CoV.[12–17] Its active metabolite, 18β-glycyrrhetinic acid (18β-GA, **2**), exerts antiviral effects by interfering with viral entry, replication, and protein synthesis, while also modulating the host immune responses.[12,18,19] Both GL and 18β-GA display significant anti-inflammatory properties by inhibiting nuclear factor-κB (NF-κB) signaling and reducing the production of pro-inflammatory cytokines, making them promising candidates with dual

[a]*Department of Biological Science and Technology, National Yang Ming Chiao Tung University, 75 Po-Ai Street, Hsinchu 30010, Taiwan, Republic of China. E-mail: tkwmll@nycu.edu.tw*

[b]*Center for Emergent Functional Matter Science, National Yang Ming Chiao Tung University, 1001 Ta-Hsueh Rd, Hsinchu 30010, Taiwan, Republic of China*

[c]*Center for Intelligent Drug Systems and Smart Bio-devices (IDS²B), National Yang Ming Chiao Tung University, 30010, Hsinchu, Taiwan, Republic of China*

antiviral and immunomodulatory functions.[20,21] During the COVID-19 pandemic, GL has emerged as a highly attractive therapeutic candidate due to its ability to target multiple stages of the SARS-CoV-2 life cycle. Studies have shown that GL can inhibit viral entry by blocking the interaction between the spike (S) protein and the angiotensin-converting enzyme 2 (ACE2) receptor, and it can also suppress viral replication by inhibiting the main protease (M^{pro}).[22–24] These multi-target mechanisms help reduce viral load and slow disease progression, further highlighting the therapeutic potential of GL and its derivatives in the treatment of COVID-19.[22–28]

Despite the promising biological activities of GL and 18β-GA, their clinical application is limited by poor aqueous solubility and instability under physiological conditions. To address these shortcomings and improve their drug-like properties, chemical modification strategies such as glycosylation and acetylation have been developed. These bioconjugation approaches can enhance solubility, hydrophilicity, metabolic stability, and overall pharmacokinetic profiles, thereby reducing the required dosages and improving target specificity.[29–31] Building upon our previous work in developing steroidal glycosides with anticancer potential, we synthesized a series of novel glycosylated derivatives based on the 18β-GA scaffold conjugating it with various monosaccharides to form glycosides.[31–33] These derivatives were evaluated for their anti-SARS-CoV-2 activity, specifically targeting the inhibition of receptor-binding domain (RBD)–ACE2 binding and M^{pro} enzymatic activity. The results showed that 18β-GA-3-*O*-β-Glc and 18β-GA-30-*O*-β-Glc exhibited significantly enhanced antiviral effects, with particularly promising inhibition of M^{pro}. Molecular docking studies further demonstrated that these glycosides have strong binding affinities for M^{pro} and adopt binding conformations similar to that of the co-crystallized M^{pro}–GC376 complex. Overall, the findings highlight the potential of 18β-GA-derived glycosides as promising COVID-19 therapeutic candidates, offering broad-spectrum antiviral activity and improved drug-like properties.

2. Results

2.1 *In vivo* one-pot synthesis and structural characterization of 18β-GA-glycosides

Enantiomerically pure 18β-GA glycosides were enzymatically synthesized by conjugating 18β-GA with various monosaccharides, including glucose (Glc), galactose (Gal), mannose (Man), 2-deoxyglucose (2-DG), and 2-deoxygalactose (2-DGal). This study employed an *in vivo* one-pot, multi-enzyme system comprising four enzymes: *N*-acetylhexosamine 1-kinase (NahK) and UDP-sugar pyrophosphorylase (BLUSP) from *Bifidobacterium longum*, inorganic pyrophosphatase (PmPpA) from *Pasteurella multocida*, and a GT-B type NDP-glycosyltransferase (Bs-YjiC) from *Bacillus subtilis*.[34–37] Previous studies have demonstrated that this system efficiently phosphorylates low-cost monosaccharides to generate sugar-1-phosphates, which are then converted into uridine diphosphate (UDP) sugars *via* conjugation with uridine triphosphate (UTP). This eliminates the need for costly UDP-sugar precursors, significantly reducing production costs. The inorganic pyrophosphate (PPi) byproduct is hydrolyzed by PmPpA into two inorganic phosphate (Pi) molecules, thereby driving the reaction forward. Glycosylation of 18β-GA with these UDP-sugars, catalyzed by Bs-YjiC, resulted in β-anomer-specific 18β-GA glycosides. Using this enzymatic one-pot approach, nine distinct 18β-GA glycosides were synthesized, including seven mono-glycosides: 18β-GA-3-*O*-β-Glc (**3**), 18β-GA-30-*O*-β-Glc (**4**), 18β-GA-3-*O*-β-Man (**6**), 18β-GA-30-*O*-β-Man (**7**), 18β-GA-30-*O*-β-Gal (**9**), 18β-GA-3-*O*-β-2-DG (**10**), and 18β-GA-3-*O*-β-2-DGal (**11**); as well as two di-glycosides: 18β-GA-3,30-*O*-β-bis-Glc (**5**) and 18β-GA-3,30-*O*-β-bis-Man (**8**) (Fig. 1).

The synthesized 18β-GA glycosides were purified by column chromatography and structurally characterized using high-resolution electrospray ionization mass spectrometry (HR-ESI-MS) and $^{1}H/^{13}C$ nuclear magnetic resonance (NMR) spectroscopy. HR-ESI-MS analysis revealed that glycosides of glucose (**3**, **4**, **5**), mannose (**6**, **7**, **8**), and galactose (**9**) formed protonated species, while those of 2-deoxyglucose (**10**) and 2-deoxygalactose (**11**) existed as sodium adducts. The glycosylation positions, stereochemistry, and configurations of both the steryl and glycosidic linkages were elucidated using comprehensive NMR techniques, including ^{1}H, ^{13}C, DEPT (90° & 135°), COSY, HSQC, HMBC, and NOE. ^{13}C NMR analysis indicated that glycosylation at the C3 position caused a downfield shift of the hydroxyl carbon from 77.3 ppm to approximately 88.3 ± 0.5 ppm, while glycosylation at the C30 position resulted in an upfield shift of the carboxyl carbon from 178.2 ppm to 175.0 ± 0.5 ppm. The structures of the 2-deoxy-Glc and 2-deoxy-Gal glycosides were confirmed by characteristic NMR signatures: in ^{1}H NMR, the H2a′ and H2b′ protons appeared at δ_H = 1.48 ppm and 2.14 ppm, respectively, and the ^{13}C NMR signals for the C2′ carbon were observed at 29.8 ppm (2-DG) and 30.1 ppm (2-DGal).

To determine the glycosylation sites and confirm the β-glycosidic linkages of the attached monosaccharides, Nuclear Overhauser Effect (NOE) experiments were conducted. Selective saturation of specific proton signals followed by observation of correlated signal enhancements enabled precise structural elucidation. For 18β-GA-3-*O*-β-Glc (**3**), saturation of the anomeric proton H1′ (δ_H = 4.30 ppm) enhanced the H5′ signal at δ_H = 3.22 ppm, confirming β-glucosidic linkage. In 18β-GA-3,30-*O*-β-bis-Glc (**5**), saturation of H1′ (δ_H = 4.30 ppm) and H1″ (δ_H = 5.56 ppm) enhanced H5′ (δ_H = 3.22 ppm) and H3″ (δ_H = 3.40 ppm), respectively, indicating successful glycosylation at both C3 and C30 positions. For 18β-GA-3-*O*-β-Man (**6**), saturation of H1′ (δ_H = 4.30 ppm) enhanced H2′ (δ_H = 3.18 ppm), confirming β-mannosidic linkage. Similarly, in 18β-GA-3,30-*O*-β-bis-Man (**8**), saturation of H1′ (δ_H = 4.30 ppm) and H1″ (δ_H = 5.49 ppm) led to enhancements of H2′ (δ_H = 3.31 ppm) and H2″ (δ_H = 3.38 ppm), respectively, supporting dual mannosylation. In 18β-GA-30-*O*-β-Gal (**9**), saturation of H1′ (δ_H = 5.46 ppm) enhanced both H5′ (δ_H = 3.62 ppm) and H4′ (δ_H = 3.53 ppm), while reciprocal enhancement upon saturation of H4′ (δ_H = 3.53 ppm) and H5′ (δ_H = 3.62 ppm) further confirmed the β-galactosidic configuration. For 18β-GA-3-*O*-β-2-DG (**10**), saturation of H1′ (δ_H = 4.57 ppm) enhanced H2′b (δ_H = 2.14 ppm) and H5′ (δ_H = 3.17 ppm); saturation of H2′b also enhanced H1′, H2′a (δ_H

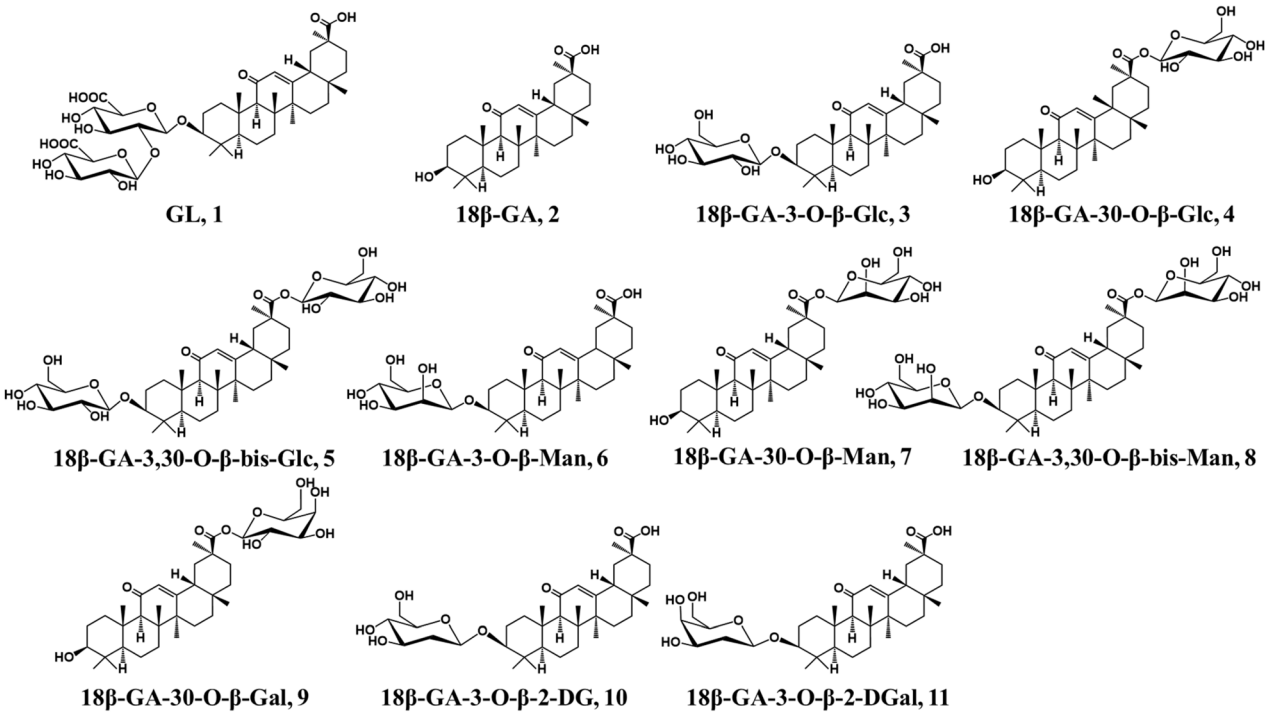

Fig. 1 Chemical structures of GL, 18β-GA, and nine 18β-GA-glycosides.

= 1.48 ppm), and H3′ (δ_H = 3.52 ppm), confirming the 2-DG structure. In the case of 18β-GA-3-*O*-β-2-deoxy-Gal (**11**), saturation of H1′ (δ_H = 4.55 ppm) enhanced H2′b (δ_H = 2.13 ppm) and H4′ (δ_H = 3.18 ppm). Saturation of H2′b enhanced H1′ and H2′a (δ_H = 1.47 ppm), while saturation of H3′ (δ_H = 3.49 ppm) led to enhancement of H4′ (δ_H = 3.18 ppm), and *vice versa*. Collectively, these NOE correlations confirm the stereospecific attachment and structural integrity of both mono- and di-glycosylated 18β-GA derivatives.

2.2 Inhibition of ACE2 binding to RBD

The inhibitory effects of GL, 18β-GA, and 18β-GA glycosides (compounds **3–11**) on the interaction between the SARS-CoV-2 spike protein receptor-binding domain (RBD) and the ACE2 receptor, as well as their inhibition of main protease (M^{pro}) activity, were evaluated to assess their antiviral potential. An enzyme-linked immunosorbent assay (ELISA) was used to measure the inhibition of RBD–ACE2 binding, with dalbavancin (50 μM in 2.5% DMSO) serving as the positive control. In this assay, ACE2 protein was immobilized onto 96-well plates, followed by the addition of test compounds (**1–11**). The SARS-CoV-2 RBD protein was then introduced, and its binding was detected using a primary anti-RBD antibody and an HRP-conjugated secondary antibody. Absorbance at 450 nm was measured, with a decrease in the signal indicating inhibition of RBD–ACE2 binding. As summarized in Table S1, dalbavancin exhibited the highest inhibition at 62.8%, outperforming all tested compounds. GL (**1**) showed moderate inhibition at 17.7%, consistent with previous reports that GL partially blocks RBD–ACE2 interaction, thereby reducing viral attachment and entry.[22–24] Several 18β-GA glycosides displayed stronger inhibition than GL, including 18β-GA-30-*O*-β-Glc (**4**, 23.8%), 18β-GA-3-*O*-β-Man (**6**, 21.3%), 18β-GA-30-*O*-β-Man (**7**, 19.3%), 18β-GA-3-*O*-β-2-DG (**10**, 29.3%), and 18β-GA-3,30-*O*-β-bis-Glc (**5**, 25.3%) (Table S1). However, none of the glycosides surpassed the inhibitory activity of dalbavancin.

2.3 Inhibitory effect of 18β-GA-glycosides on M^{pro}

The inhibitory activity of 18β-GA glycosides against SARS-CoV-2 M^{pro} was evaluated using a Förster resonance energy transfer (FRET)-based assay with a fluorogenic peptide substrate. The assay utilized a 14-mer peptide (DABCYL–KTSAVLQSGFRKME–EDANS), in which cleavage by M^{pro} separates the DABCYL (quencher) and EDANS (fluorophore) moieties, resulting in increased fluorescence at 460 nm upon excitation at 355 nm, indicating enzymatic activity. Compounds **1–11** were tested, with GC376 as a positive control. Initial screening was conducted at 50 μM. Compounds that retained more than 50% M^{pro} inhibition at this concentration were subjected to a dose–response analysis using two-fold serial dilutions (50, 25, 12.5, 6.25, 3.125, 1.5625, 0.78125, and 0.3906 μM) to determine their half-maximal inhibitory concentration (IC_{50}) values. Among the tested compounds, 18β-GA (**2**), 18β-GA-3-*O*-β-Glc (**3**), 18β-GA-30-*O*-β-Glc (**4**), and 18β-GA-30-*O*-β-Man (**7**) demonstrated significant inhibitory activity, with IC_{50} values of 23.12 ± 3.29 μM, 8.70 ± 0.80 μM, 4.77 ± 0.49 μM, and 32.46 ± 7.28 μM, respectively (Table S2). Among these, compound **4** exhibited the most potent M^{pro} inhibition, as shown in Fig. 2.

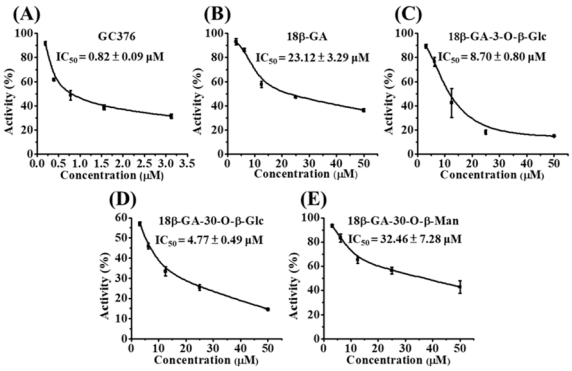

Fig. 2 Analysis of the inhibitory effect of 18β-GA glycosides on the enzymatic activity of M^{pro} of SARS-CoV-2. (A) GC376; (B) 18β-GA; (C) 18β-GA-3-*O*-β-Glc; (D) 18β-GA-30-*O*-β-Glc; (E) 18β-GA-30-*O*-β-Man.

2.4 Binding affinity assays of 18β-GA-3-*O*-β-Glc and 18β-GA-30-*O*-β-Glc to M^{pro}

The binding interactions of compounds **3** and **4** with SARS-CoV-2 M^{pro} were assessed using real-time, label-free biolayer interferometry (BLI). As shown in Fig. 3, both compounds exhibited similar binding kinetics. During the 150-second association phase, they rapidly (≤50 s) and logarithmically bound to the M^{pro}-immobilized probe, reaching a steady-state plateau. In the subsequent dissociation phase, both compounds displayed a rapid release within the first 5 seconds. The equilibrium dissociation constants ($K_D = k_{off}/k_{on}$) were calculated as 2.76×10^{-4} M for compound **3** and 1.76×10^{-5} M for compound **4** (Fig. 3). These findings indicate that both compounds are reversible inhibitors of M^{pro}, with compound **4** demonstrating significantly stronger binding affinity.

2.5 Pharmacological and bioavailability of 18β-GA glycosides

The pharmacokinetic potential of the synthesized 18β-GA glycosides was evaluated using the SwissADME platform, focusing on key physicochemical and bioavailability parameters (Table 1).[38] According to Lipinski's Rule of Five (RO5), an orally active drug typically meets the following criteria: molecular weight (MW) ≤ 500 Da, hydrogen bond acceptors (HBA) < 10, hydrogen bond donors (HBD) ≤ 5, and lipophilicity (Mlog P ≤ 4.15). All eleven tested compounds exceeded the MW threshold, and the two di-glycosylated derivatives, compound **5** (18β-GA-3,30-*O*-β-bis-Glc) and compound **8** (18β-GA-3,30-*O*-β-bis-Man), also surpassed the limits for both HBA and HBD. Despite these violations, several glycosides demonstrated favorable predicted oral bioavailability. This may be attributed to compensatory factors such as intramolecular hydrogen bonding, increased molecular rigidity, or formulation strategies that reduce polar surface area and enhance membrane permeability.[39–42] Notably, the mono-glycosylated compound **4** (18β-GA-30-*O*-β-Glc) showed a higher bioavailability score than compound **3** (18β-GA-3-*O*-β-Glc), alongside superior inhibitory activity against M^{pro}, suggesting its potential as an orally available antiviral agent at lower doses. These findings support the broader perspective that Lipinski's rule of five should be interpreted as a flexible guideline rather than an absolute rule. Many clinically approved drugs violate one or more RO5 criteria yet remain pharmacologically effective due to unique structural attributes and specialized mechanisms. For example, cyclosporin A (~1202 Da) remains orally bioavailable due to its cyclic structure, which reduces polarity and facilitates membrane transport. Similarly, antibiotics such as erythromycin (~734 Da) and vancomycin (~1449 Da) exceed the MW limit but are therapeutically active through targeted bacterial interactions.[43] Other notable exceptions include atorvastatin (Lipitor), which violates log P criteria, and rifampin (~822 Da), an effective anti-tuberculosis agent. These examples illustrate that drug-likeness can be achieved through alternative strategies such as active transport, prodrug design, and conformational restriction, further reinforcing the therapeutic potential of 18β-GA glycosides as viable antiviral candidates.

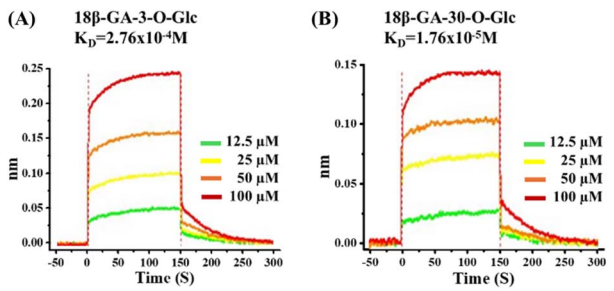

Fig. 3 BLI results of 18β-GA-3-*O*-β-Glc and 18β-GA-30-*O*-β-Glc with M^{pro}. (A) 18β-GA-3-*O*-β-Glc; (B) 18β-GA-30-*O*-β-Glc.

2.6 Molecular docking of 18β-GA glycosides and M^{pro}

Molecular docking studies were performed to investigate the interactions between SARS-CoV-2 M^{pro} and the effective 18β-GA glycoside inhibitors, 18β-GA, 18β-GA-3-*O*-β-Glc, and 18β-GA-30-*O*-β-Glc, with a focus on their binding within the protease's active site. To validate the docking methodology, simulations were first conducted using GC376, a well-established M^{pro} inhibitor, and the results were compared with the reported crystal structure of the GC376–M^{pro} complex (PDB: 6W63). The simulated binding conformation closely matched the crystallographic data, replicating key electrostatic, hydrogen-bonding, and hydrophobic interactions, thus confirming the reliability of the docking protocol. The GC376–M^{pro} complex features a catalytic dyad (Cys145–His41) and four substrate-binding pockets (S1–S4). The S1 pocket, comprising His163 and Glu166, accommodates a P1 glutamine; the hydrophobic S2 pocket (His41, Met49, Met165) binds P2 leucine; the shallow S3 pocket (Thr24, Thr26, Asn142) interacts with small polar groups; and the large, hydrophobic S4 pocket (Met165, Leu167, Pro168) fits bulky residues like valine. GC376 demonstrated strong binding affinity (−148.4 kJ mol^{-1}), with its P1 glutamine surrogate forming hydrogen bonds with Asn142 (S3) and its sulfite group at P2 engaging Ser144 and Cys145. The P2 nitrogen formed van der Waals contacts with Glu166 (S1), and the P3

Table 1 Physico-chemical properties of the synthesized 18β-GA compounds in terms of SwissADME parameters

	Lipinski's rules					
Compounds	MW ≤ 500	HBA < 10	HBD ≤ 5	Mlog P ≤ 4.15	Lipinski's violations	Bioavailability score
GL (**1**)	822.93	16	8	0.02	3	0.11
18β-GA (**2**)	470.68	3	2	4.87	1	0.85
18β-GA-3-*O*-β-Glc (**3**)	632.82	9	5	2.38	1	0.11
18β-GA-30-*O*-β-Glc (**4**)	632.82	9	5	2.38	1	0.55
18β-GA-3,30-*O*-β-bis-Glc (**5**)	794.97	14	8	0.04	3	0.17
18β-GA-3-*O*-β-Man (**6**)	632.82	9	5	2.38	1	0.11
18β-GA-30-*O*-β-Man (**7**)	632.82	9	5	2.38	1	0.55
18β-GA-3,30-*O*-β-bis-Man (**8**)	794.97	14	8	0.04	3	0.17
18β-GA-30-*O*-β-Gal (**9**)	632.82	9	5	2.38	1	0.55
18β-GA-3-*O*-β-2DG (**10**)	616.83	8	4	3.16	1	0.56
18β-GA-3-*O*-β-2DGal (**11**)	616.83	8	4	3.16	1	0.56

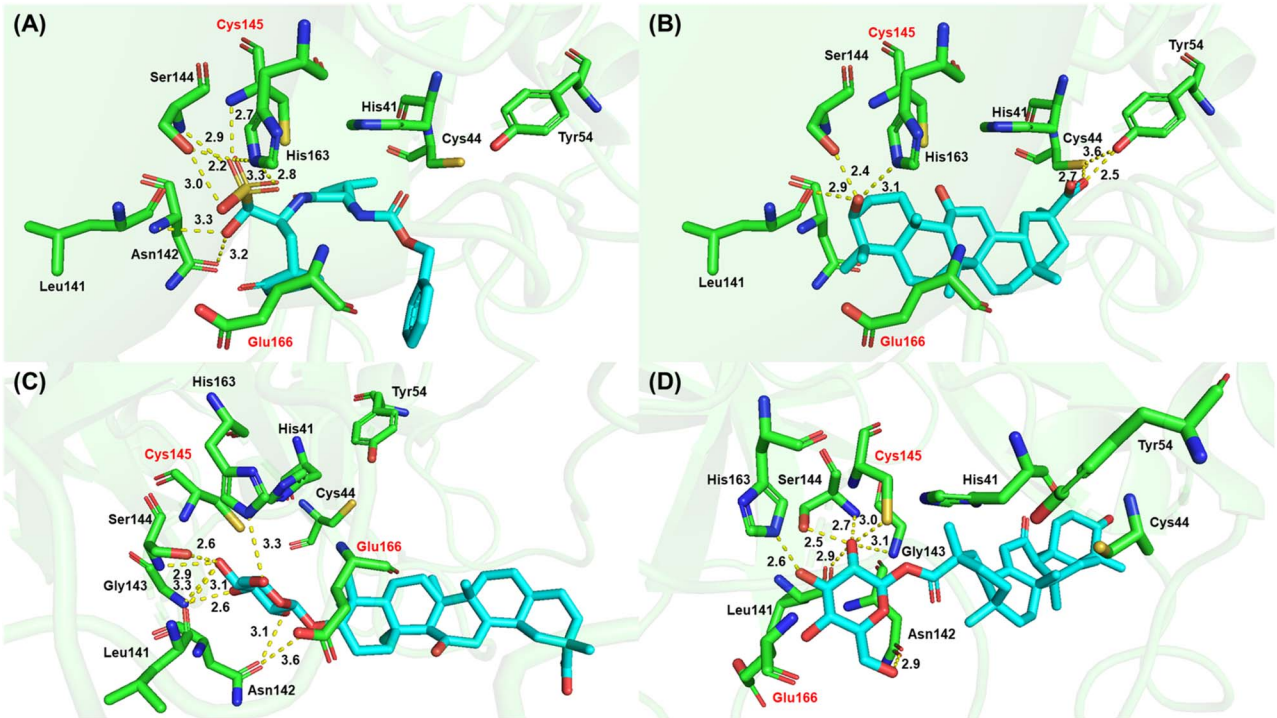

Fig. 4 Molecular docking results of 18β-GA and derivatives with M^{pro} (PDB: 6W63). (A) GC376; (B) 18β-GA; (C) 18β-GA-3-*O*-β-Glc; (D) 18β-GA-30-*O*-β-Glc.

benzyl ring established a hydrogen bond with His163 (S1), further validating the robustness of the docking setup (Fig. 4A). Docking of 18β-GA revealed a binding energy of −104.9 kJ mol^{-1}. The hydroxyl group at the C3 position of the A ring formed hydrogen bonds with Leu141, Ser144, and His163, while the carboxylic acid on the E ring interacted with Cys44 and Tyr54 (Fig. 4B). For 18β-GA-3-*O*-β-Glc, the glucose moiety extended into the substrate-binding pocket, enhancing binding energy to −124.8 kJ mol^{-1}. Its glycosyl hydroxyl groups formed hydrogen bonds with Leu141, Asn142, Gly143, Ser144, Cys145, and Glu166 (Fig. 4C). Notably, 18β-GA-30-*O*-β-Glc showed the strongest binding among the glycosides (−131.78 kJ mol^{-1}), with interactions involving the same key residues. Additionally, the C30 carboxyl group formed a unique hydrogen bond with Asn142, further enhancing complex stability (Fig. 4D). Collectively, these results demonstrate that glycosylation of 18β-GA significantly improves its binding affinity toward M^{pro}, likely due to enhanced hydrogen bonding and active site engagement. This supports the potential of glycosylated 18β-GA derivatives as promising M^{pro} inhibitors for COVID-19 therapeutics.

3. Discussion

The COVID-19 pandemic has underscored the urgent need for effective antiviral therapies. SARS-CoV-2, the virus responsible for COVID-19, infects human alveolar cells *via* the ACE2

receptor, triggering severe immune responses that can lead to cytokine storms, the accumulation of reactive oxygen species (ROS), excessive airway secretions, hypoxia, and organ failure. Targeting the viral M^{pro}, which is essential for viral replication, has emerged as a promising therapeutic strategy. M^{pro} inhibitors, such as GC376, are designed to mimic the P1–P4 residues of the viral polyprotein substrate to enhance binding specificity and affinity. Originally developed for feline infectious peritonitis coronavirus (FIPV), GC376 features a glutamine surrogate at the P1 position and exhibits potent M^{pro} inhibition with a reported IC_{50} of 0.15 ± 0.03 μM.[39,44] However, side effects observed in animal studies, such as delayed adult tooth development, have prevented its FDA approval.

In the search for effective SARS-CoV-2 treatments, various M^{pro} inhibitors have been developed or repurposed, each with differing efficacy, safety, and cost profiles. Among them, nirmatrelvir, the active component of Paxlovid, has demonstrated potent antiviral activity, with an IC_{50} of 19.2 nM against M^{pro}.[4] However, it requires co-administration with ritonavir to extend its half-life, increasing the risk of drug–drug interactions. Additionally, its high cost—approximately $530 per treatment course in the U.S., limits global accessibility, though generic versions ($25–50) are available in low-income regions through the Medicines Patent Pool. Newer M^{pro} inhibitors, such as TKB272, have shown even potency (IC_{50} of 0.7 μM) and offer advantages including the avoidance of off-target toxicity and no need for a pharmacokinetic booster. Despite these benefits, challenges related to clinical validation, safety assessment, large-scale manufacturing, and affordability remain significant obstacles to their widespread use.[45] Meanwhile, several repurposed drugs, such as ethacrynic acid, naproxen, and raloxifene hydrochloride, offer low-cost alternatives but lack comprehensive clinical validation.[46] Although these compounds show promising antiviral activity, their utility is limited by poor bioavailability and potential toxicity, highlighting the importance of formulation optimization in antiviral drug development. In contrast to synthetic M^{pro} inhibitors such as Paxlovid (nirmatrelvir/ritonavir), TKB272, and GC376, GL and its active metabolite 18β-GA offer broader-spectrum antiviral activity and potential cost-effectiveness.[47] Unlike pathogen-specific antivirals, GL and 18β-GA exhibit activity against a wide range of viruses, potentially reducing the risk of resistance. Their dual antiviral and anti-inflammatory properties are particularly beneficial for mitigating the cytokine storms associated with severe COVID-19. However, their clinical application is hampered by poor oral bioavailability, low aqueous solubility, and rapid metabolic degradation, necessitating innovative formulation strategies to unlock their full therapeutic potential.

In this study, we employed a glycosylated prodrug strategy to generate 18β-GA glycosides using a one-pot, multi-enzyme system, which significantly improved their solubility, bioavailability, and antiviral efficacy against SARS-CoV-2 M^{pro}. Glycosylation not only optimized pharmacokinetic properties but also enhanced target specificity through improved interactions with viral proteins and host transport mechanisms. Nevertheless, the *in vivo* stability of glycosides remains a major challenge, as glycosidic bonds are often susceptible to hydrolysis by host glycosidases and intestinal microbiota, potentially limiting systemic exposure. To address this, future studies should evaluate their metabolic stability and pharmacokinetics in animal models and explore strategies such as resistant C-glycosides or protective delivery systems (*e.g.*, nanoparticles, liposomes). These approaches will be crucial to ensure sufficient *in vivo* persistence and to confirm the therapeutic potential of 18β-GA glycosides as anti-SARS-CoV-2 candidates.

Molecular docking results revealed that 18β-GA-3-*O*-β-Glc (**3**) and 18β-GA-30-*O*-β-Glc (**4**) are promising M^{pro} inhibitors, with their sugar moieties playing a key role in engaging the enzyme's active site. Glycosylation not only preserved critical interactions within the S1/S2 subsites of M^{pro} but also introduced additional interactions, such as with Asn142, which are not typically observed in canonical inhibitors like GC376. These shifts in binding patterns suggest that sugar conjugation may provide a tunable strategy to optimize molecular recognition, stability, and potency. Further exploration of alternative sugar types or attachment positions could facilitate the development of next-generation GA-derived inhibitors with enhanced antiviral efficacy. In addition, although further *in vitro* and *in vivo* validation is warranted, existing evidence indicates that glycosylation can direct drugs toward specific proteins or transporters that recognize glycosylated structures, thereby improving both target specificity and therapeutic efficacy. This approach is supported by precedents in clinically approved antiviral drugs. For instance, zanamivir, a neuraminidase inhibitor used for influenza, mimics the enzyme's natural sialic acid substrate, enabling precise binding and inhibition.[45] Similarly, ribavirin, a broad-spectrum antiviral, uses its sugar moiety to facilitate cellular uptake *via* nucleoside transporters and is metabolized into active forms that suppress viral replication.[48] These examples underscore the importance of glycosylation in antiviral drug development and highlight its potential for optimizing 18β-GA derivatives into cost-effective and targeted M^{pro} inhibitors.

4. Conclusions

This study proposes a promising and cost-effective strategy for developing SARS-CoV-2 M^{pro} inhibitors by repurposing 18β-GA, a natural metabolite of glycyrrhizin. Using a one-pot, four-enzyme biosynthetic system (NahK, BLUSP, PmPpA, and Bs-YjiC), we efficiently synthesized two glycosylated derivatives, 18β-GA-3-*O*-β-Glc and 18β-GA-30-*O*-β-Glc, which exhibited potent M^{pro} inhibitory activity, with IC_{50} values of 8.70 ± 0.80 μM and 4.77 ± 0.49 μM, respectively. Biolayer interferometry (BLI) analysis showed comparable binding affinities and distinct kinetic profiles, suggesting different interaction dynamics with M^{pro}. Molecular docking confirmed binding at the M^{pro} active site, indicating possible covalent interactions similar to the known inhibitor GC376. Glycosylation not only enhanced the aqueous solubility and binding affinity of 18β-GA but also offers a sustainable, enzyme-based synthesis route consistent with green chemistry principles, supporting scalability and environmental compatibility. However, this study is limited to *in vitro* assays. Further research should involve *in vivo*

validation using SARS-CoV-2 animal models to assess therapeutic efficacy, toxicity, and immunomodulatory effects. Further investigation into the compounds' pharmaceutics and bioavailability, including ADME properties, is also needed. Structural studies such as X-ray crystallography are warranted to confirm binding modes and assess potential off-target effects. In addition, structural modifications of the glycoside moiety (*e.g.*, branching, acetylation, or sulfation) may enhance potency, stability, and cellular permeability. In conclusion, glycosylated 18β-GA derivatives represent a viable class of natural product-based M^{pro} inhibitors with strong translational potential. With further validation and optimization, they could serve as affordable therapeutic options for COVID-19, especially in resource-limited settings.

5. Experimental section

5.1 Construction of NahK–PmPpA and Bs-YjiC–BLUSP duet plasmids

The *NahK*, *BLUSP*, *PmPpA*, and *Bs-YjiC* genes were synthesized by GenScript Biotech and initially cloned into individual plasmid vectors. These vectors were transformed into *E. coli* XL1-Blue cells for plasmid amplification. Following amplification, each gene was excised from its respective vector using appropriate restriction enzymes and ligated into the pETDuet-1 and pCOLADuet-1 vectors to construct two dual-expression plasmids: pETDuet-1–Bs-YjiC–BLUSP and pCOLADuet-1–NahK–PmPpA. These plasmids were designed to enable the co-expression of two enzymes per plasmid. The two plasmids were co-transformed into *E. coli* BL21(DE3) cells to generate an engineered strain capable of *in vivo*, one-pot biosynthesis of 18β-GA glycosides. The pCOLADuet-1 plasmid confers kanamycin resistance, while pETDuet-1 carries an ampicillin resistance marker. Successful co-transformation and plasmid retention were initially verified by screening on LB agar plates containing both antibiotics. The presence of all four target genes in the engineered *E. coli* BL21(DE3) strain was further confirmed by DNA sequencing.

5.2 One-pot synthesis of 18β-GA-glycosides

An *in vivo* one-pot synthesis method was employed to produce 18β-GA glycosides. *E. coli* BL21(DE3) cells co-expressing NahK, PmPpA, Bs-YjiC, and BLUSP were cultured in 500 mL of LB medium at 37 °C until the optical density at 600 nm (OD_{600}) reached 0.6. Protein expression was induced with 0.2 mM IPTG, followed by incubation for an additional 20 hours at 28 °C. After induction, cells were harvested by centrifugation and resuspended in 30 mL of M9 medium supplemented with 400 mg of various monosaccharides (*e.g.*, glucose, galactose, mannose, 2-deoxyglucose, and 2-deoxygalactose) and 20 mg of 18β-GA. The reaction mixture was incubated at 37 °C for 16 hours to facilitate glycoside formation. Following incubation, the mixture was extracted with an equal volume of ethyl acetate, in which the synthesized 18β-GA glycosides were partitioned into the organic phase. The products were initially analyzed by thin-layer chromatography (TLC), purified by high-performance liquid chromatography (HPLC), and structurally characterized by high-resolution electrospray ionization mass spectrometry (HR-ESI-MS) and nuclear magnetic resonance (NMR) spectroscopy.

5.2.1 18β-GA-3-*O*-β-Glc (3). ^{1}H NMR (700 MHz, methanol-d_4, CD_3OD): δ 5.56 (s, 1H, H-12), 4.30 (d, J = 7.8 Hz, 1H, H-1′), 3.82 (dd, J = 11.8, 2.3 Hz, 1H, H-6′b), 3.65 (dd, J = 11.8, 5.5 Hz, 1H, H-6′b), 3.17 (m, 1H, H-2′), 3.31 (m, 1H, H-3′), 3.26 (m, 1H, H-4′), 3.22 (m, 1H, H-5′), 2.69 (dt, J = 13.6, 3.7 Hz, 1H, H-1a), 2.44 (s, 1H, H-9), 2.21–2.10 (m, 1H, H-16b), 1.84–1.93 (m, 2H, H-21b, H-19b), 1.92–1.80 (m, 2H, H-2b, H-15b), 1.78–1.67 (m, 3H, H-2a, H-7b, H-19a), 1.64–1.58 (m, 1H, H-6b), 1.50–1.42 (m, 1H, H-22a), 1.31–1.21 (m, 1H, H-15a), 1.16 (s, 3H, H-29), 1.13 (d, 6H, H-25, H-26), 0.82 (s, 3H, H-24), 0.86 (s, 3H, H-28), 1.41 (s, 3H, H-27), 0.81–0.76 (m, 1H, H-5), 1.05–0.97 (m, 2H, H-1b, H-16a), 3.21–3.15 (m, 1H, H-3), 1.46–1.35 (m, 4H, H-6a, H-7a, H-22b, H-21a), 2.17–2.20 (m, 1H, H-18), 1.06 (s, 3H, H-23). ^{13}C NMR (175 MHz, methanol-d_4, CD_3OD): δ 38.1 (C-1), 25.4 (C-2), 88.3 (C-3), 38.4 (C-4), 54.3 (C-5), 16.3 (C-6), 31.7 (C-7), 44.6 (C-8), 61.0 (C-9), 35.9 (C-10), 200.5 (C-11), 126.8 (C-12), 170.7 (C-13), 42.8 (C-14), 25.4 (C-15), 25.2 (C-16), 30.8 (C-17), 47.8 (C-18), 40.3 (C-19), 42.8 (C-20), 29.9 (C-21), 36.9 (C-22), 26.6 (C-23), 14.8 (C-24), 14.8 (C-25), 17.1 (C-26), 21.7 (C-27), 27.0 (C-28), 26.6 (C-29), 178.3 (C-30), 104.6 (C-1′), 60.6 (C-6′), 75.6 (C-5′), 69.5 (C-4′), 76.1 (C-3′), 73.5 (C-2′). The calculated ESI-HRMS of 18β-GA-3-*O*-β-Glc ($C_{36}H_{56}O_9$) was 632.3924 g mol^{-1}. The experimental peak of m/z = 633.3997 was considered as $[M + H]^+$.

5.2.2 18β-GA-30-*O*-β-Glc (4). ^{1}H NMR (700 MHz, methanol-d_4, CD_3OD): δ 5.60 (s, 1H, H-12), 5.50 (d, J = 8.2 Hz, 1H, H-1′), 3.84 (dd, J = 12.1, 2.1 Hz, 1H, H-2′b), 3.69 (dd, J = 12.0, 4.9 Hz, 1H, H-6′b), 3.16 (dd, J = 11.9, 4.5 Hz, 1H, H-3), 3.31 (m, 1H, H-2′), 3.41 (m, 1H, H-3′), 3.39 (m, 1H, H-4′), 3.37 (m, 1H, H-5′), 2.71 (dt, J = 13.5, 3.6 Hz, 1H, H-1a), 1.05–0.98 (m, 2H, H-1b, H-16a), 2.44 (s, 1H, H-9), 2.17–2.10 (m, 1H, H-16b), 1.77–1.70 (m, 2H, H-2b, H-19a), 1.91–1.83 (m, 2H, H-2b, H-19b), 0.79 (s, 3H, H-24), 0.82 (s, 3H, H-28), 0.98 (s, 3H, H-23), 1.13 (s, 6H, H-25, H-26), 1.19 (s, 3H, H-29), 1.41 (s, 3H, H-27), 1.92–1.87 (m, 1H, H-15b), 1.31–1.21 (m, 1H, H-15a), 2.23 (m, 1H, H-18), 1.64–1.58 (m, 1H, H-6b), 1.49–1.35 (m, 4H, H-6a, H-7a, H-22b, H-21a), 0.75 (dd, J = 12.0, 1.9 Hz, 1H, H-5), 1.72–1.68 (m, 1H, H-7b), 1.50–1.42 (m, 1H, H-22a), 2.02–1.98 (m, 1H, H-21b). ^{13}C NMR (175 MHz, methanol-d_4, CD_3OD): δ 38.9 (C-1), 30.4 (C-2), 78.0 (C-3), 38.8 (C-4), 54.7 (C-5), 17.2 (C-6), 32.4 (C-7), 45.3 (C-8), 61.7 (C-9), 36.9 (C-10), 201.3 (C-11), 127.5 (C-12), 171.4 (C-13), 43.8 (C-14), 26.0 (C-15), 26.1 (C-16), 31.5 (C-17), 48.4 (C-18), 40.9 (C-19), 43.8 (C-20), 30.5 (C-21), 37.2 (C-22), 27.2 (C-23), 15.5 (C-24), 14.9 (C-25), 17.8 (C-26), 22.3 (C-27), 27.5 (C-28), 26.7 (C-29), 175.5 (C-30), 94.3 (C-1′), 61.1 (C-6′), 76.9 (C-5′), 69.8 (C-4′), 77.5 (C-3′), 72.7 (C-2′). The calculated ESI-HRMS of 18β-GA-30-*O*-β-Glc ($C_{36}H_{56}O_9$) was 632.3924 g mol^{-1}. The experimental peak of m/z = 633.3997 was considered as $[M + H]^+$.

5.2.3 18β-GA-3,30-*O*-β-bis-Glc (5). ^{1}H NMR (700 MHz, methanol-d_4, CD_3OD): δ 5.66 (s, 1H, H-12), 4.37 (d, J = 7.8 Hz, 1H, H-1′), 3.85 (dd, J = 11.9 Hz, 1H, H-6′b), 3.72 (dd, J = 11.9, 5.5 Hz, 1H, H-6′b), 3.24 (m, 1H, H-2′), 3.37 (m, 1H, H-3′), 3.42 (m, 1H, H-4′), 3.30 (m, 1H, H-5′), 5.56 (d, J = 8.2 Hz, 1H, H-1″), 3.28 (m, 1H, H-2″), 3.40 (m, 1H, H-3″), 3.36 (m, 1H, H-4″), 3.46 (m, 1H, H-5″), 3.75 (dd, J = 11.9, 5.5 Hz, 1H, H-6″a), 3.88 (dd,

1H, H-6″b), 2.76 (t, J = 3.7 Hz, 1H, H-1a), 2.10–2.05 (m, 1H, H-16b), 1.33–1.27 (m, 1H, H-15a), 2.51 (s, 1H, H-9), 1.93–1.96 (m, 3H, H-21b, H-19b, H-15b), 1.93–1.96 (m, 1H, H-2b), 1.82–1.67 (m, 3H, H-2a, H-7b, H-19a), 1.53–1.59 (m, 1H, H-6b), 1.46–1.39 (m, 1H, H-22a), 1.31–1.21 (m, 1H, H-15a), 1.26 (s, 3H, H-29), 1.20 (d, 6H, H-25, H-26), 0.88 (s, 3H, H-24), 0.93 (s, 3H, H-28), 1.47 (s, 3H, H-27), 0.87–0.83 (m, 1H, H-5), 1.04–1.08 (m, 2H, H-1b, H-16a), 3.23–3.25 (m, 1H, H-3), 1.51–1.39 (m, 4H, H-6a, H-7a, H-22b, H-21a), 2.34–2.27 (m, 1H, H-18), 1.13 (s, 3H, H-23). ^{13}C NMR (175 MHz, methanol-d_4, CD_3OD): δ 38.2 (C-1), 25.5 (C-2), 88.4 (C-3), 38.3 (C-4), 54.4 (C-5), 16.3 (C-6), 31.7 (C-7), 44.7 (C-8), 61.1 (C-9), 38.4 (C-10), 200.7 (C-11), 126.9 (C-12), 170.8 (C-13), 43.1 (C-14), 25.5 (C-15), 25.4 (C-16), 30.9 (C-17), 47.8 (C-18), 40.2 (C-19), 42.5 (C-20), 29.9 (C-21), 36.5 (C-22), 26.4 (C-23), 14.9 (C-24), 14.9 (C-25), 17.2 (C-26), 21.7 (C-27), 26.9 (C-28), 26.1 (C-29), 174.9 (C-30), 104.6 (C-1′), 60.7 (C-6′), 69.6 (C-5′), 76.9 (C-4′), 76.2 (C-3′), 73.6 (C-2′), 93.6 (C-1″), 60.5 (C-6″), 76.2 (C-5″), 72.0 (C-4″), 69.2 (C-3″), 75.6 (C-2″). The calculated ESI-HRMS of 18β-GA-3,30-*O*-β-bis-Glc ($C_{42}H_{66}O_{14}$) was 794.4453 g mol^{-1}. The experimental peak of m/z = 795.4525 was considered as $[M + H]^+$.

5.2.4 18β-GA-3-*O*-β-Man (6). ^{1}H NMR (700 MHz, methanol-d_4, CD_3OD): δ 5.57 (s, 1H, H-12), 4.30 (d, J = 7.8 Hz, 1H, H-1′), 3.82 (dd, J = 11.8, 2.3 Hz, 1H, H-6′b), 3.64 (dd, J = 11.9, 5.5 Hz, 1H, H-6′b), 3.18 (d, J = 4.1 Hz, 2H, H-3, H-2′), 3.32 (m, 1H, H-3′), 3.23 (m, 1H, H-4′), 3.22 (m, 1H, H-5′), 2.68 (dt, J = 13.5, 3.7 Hz, 1H, H-1a), 2.43 (s, 1H, H-9), 2.22–2.16 (m, 1H, H-16b), 1.96–1.80 (m, 4H, H-21b, H-19b, H-15b, H-2b), 1.63–1.58 (m, 1H, H-6b), 1.50–1.42 (m, 4H, H-21a, H-22b, H-7a, H-6a), 0.81 (s, 3H, H-24), 0.85 (s, 3H, H-28), 1.40 (s, 3H, H-27), 1.07 (s, 3H, H-23), 1.12 (d, 3H, H-25), 1.13 (d, 3H, H-26), 1.14 (s, 3H, H-29), 1.77–1.65 (m, 3H, H-2a, H-7b, H-19a), 0.79–0.76 (m, 1H, H-5), 1.05–0.97 (m, 2H, H-1b, H-16a), 2.17–2.21 (m, 1H, H-18), 1.36–1.21 (m, 1H, H-15a). ^{13}C NMR (175 MHz, methanol-d_4, CD_3OD): δ 41.0 (C-1), 26.9 (C-2), 88.9 (C-3), 40.9 (C-4), 55.0 (C-5), 17.8 (C-6), 32.3 (C-7), 45.2 (C-8), 61.6 (C-9), 39.0 (C-10), 201.2 (C-11), 127.4 (C-12), 171.4 (C-13), 43.1 (C-14), 27.3 (C-15), 26.9 (C-16), 32.3 (C-17), 48.4 (C-18), 31.5 (C-19), 43.5 (C-20), 31.4 (C-21), 39.0 (C-22), 27.7 (C-23), 16.9 (C-24), 15.5 (C-25), 17.8 (C-26), 22.3 (C-27), 27.3 (C-28), 26.9 (C-29), 179.2 (C-30), 105.2 (C-1′), 74.1 (C-2′), 76.2 (C-3′), 70.1 (C-4′), 76.7 (C-5′), 61.3 (C-6′). The calculated ESI-HRMS of 18β-GA-3-*O*-β-Man ($C_{36}H_{56}O_9$) was 632.3924 g mol^{-1}. The experimental peak of m/z = 633.3997 was considered as $[M + H]^+$.

5.2.5 18β-GA-30-*O*-β-Man (7). ^{1}H NMR (700 MHz, methanol-d_4, CD_3OD): δ 5.61 (s, 1H, H-12), 5.46 (d, J = 8.2 Hz, 1H, H-1), 3.16 (dd, J = 11.8, 4.5 Hz, 1H, H-3), 2.71 (dt, J = 13.4, 3.6 Hz, 1H, H-1a), 2.43 (s, 1H, H-9), 2.14 (td, J = 13.7, 4.6 Hz, 1H, H-16b), 0.79 (s, 3H, H-24), 0.98 (s, 3H, H-23), 1.19 (s, 3H, H-29), 0.81 (s, 3H, H-28), 1.41 (s, 3H, H-27), 1.12 (s, 6H, H-25, H-26), 1.77–1.70 (m, 2H, H-2b, H-19a), 1.64–1.58 (m, 1H, H-6b), 2.27–2.22 (m, 1H, H-18), 1.26–1.20 (m, 1H, H-15a), 1.05–0.98 (m, 2H, H-1b, H-16a), 1.89–1.84 (m, 2H, H-2b, H-19b), 1.90–1.88 (m, 1H, H-15b), 1.68–1.72 (m, 1H, H-19a), 0.75 (dd, 1H, H-5), 1.49–1.35 (m, 4H, H-6a, H-7a, H-22b, H-21a), 1.50–1.42 (m, 1H, H-22a), 2.03–2.00 (m, 1H, H-21b), 1.72–1.68 (m, 1H, H-7b), 3.89 (dd, J = 3.4, 1.1 Hz, 1H, H-6′b), 3.66 (dd, J = 9.7, 8.2 Hz, 1H, H-6′a), 3.64 (m, 1H, H-2′), 3.72 (m, 1H, H-3′), 3.53 (m, 1H, H-4′), 3.62 (m, 1H, H-5′), 1.64–1.58 (m, 1H, H-6b), 0.75 (dd, J = 12.0, 1.9 Hz, 1H, H-5), 3.89 (dd, J = 12.1, 2.1 Hz, 1H, H-2′b), 3.66 (dd, J = 12.0, 4.9 Hz, 1H, H-6′a). ^{13}C NMR (175 MHz, methanol-d_4, CD_3OD): δ 40.2 (C-1), 30.8 (C-2), 77.3 (C-3), 40.2 (C-4), 54.0 (C-5), 17.1 (C-6), 32.7 (C-7), 44.6 (C-8), 61.0 (C-9), 36.5 (C-10), 200.6 (C-11), 126.8 (C-12), 170.7 (C-13), 43.1 (C-14), 26.0 (C-15), 26.5 (C-16), 31.7 (C-17), 47.4 (C-18), 42.4 (C-19), 43.2 (C-20), 30.8 (C-21), 38.1 (C-22), 26.8 (C-23), 14.2 (C-24), 14.7 (C-25), 17.1 (C-26), 21.6 (C-27), 28.6 (C-28), 26.5 (C-29), 174.8 (C-30), 93.6 (C-1′), 61.1 (C-6′), 76.9 (C-5′), 69.8 (C-4′), 77.5 (C-3′), 72.7 (C-2′). The calculated ESI-HRMS of 18β-GA-30-*O*-β-Gal ($C_{36}H_{56}O_9$) was 632.3924 g mol^{-1}. The experimental peak of m/z = 633.3997 was considered as $[M + H]^+$.

5.2.6 18β-GA-3,30-*O*-β-bis-Man (8). ^{1}H NMR (700 MHz, methanol-d_4, CD_3OD): δ 5.59 (s, 1H, H-12), 4.30 (d, J = 7.8 Hz, 1H, H-1′), 3.82 (dd, J = 11.9, 5.5 Hz, 1H, H-6′b, H-6″b), 3.66 (ddd, J = 26.7, 12.0, 5.2 Hz, 2H, H-6′a, H-6″a), 5.49 (dd, J = 8.2, 1.0 Hz, 1H, H-1″), 3.38 (m, 1H, H-2″), 3.34 (m, 1H, H-3″), 3.29 (m, 2H, H-4″), 3.30 (m, 1H, H-5″), 3.17 (m, 1H, H-2′), 3.31 (m, 1H, H-3′), 3.36 (m, 1H, H-4′), 3.20 (m, 1H, H-5′), 2.72 (t, J = 3.7 Hz, 1H, H-1a), 1.33–1.27 (m, 1H, H-15a), 2.43 (s, 1H, H-9), 2.02–1.97 (m, 2H, H-19b, H-21b), 1.92–1.94 (m, 2H, H-2b, H-15b), 2.16–2.12 (m, 1H, H-16b), 1.82–1.67 (m, 3H, H-2a, H-7b, H-19a), 1.63–1.58 (m, 1H, H-6b), 1.42–1.39 (m, 1H, H-22a), 1.18 (s, 3H, H-29), 1.12 (d, 6H, H-25, H-26), 0.81 (s, 3H, H-24), 0.85 (s, 3H, H-28), 1.40 (s, 3H, H-27), 1.05 (s, 3H, H-23), 1.04–1.09 (m, 2H, H-1b, H-16a), 1.51–1.39 (m, 4H, H-6a, H-7a, H-22b, H-21a), 2.25–2.20 (m, 1H, H-18), 0.77 (d, J = 11.8 Hz, 1H, H-5). ^{13}C NMR (175 MHz, methanol-d_4, CD_3OD): δ 38.1 (C-1), 25.4 (C-2), 88.3 (C-3), 38.3 (C-4), 54.3 (C-5), 16.3 (C-6), 31.7 (C-7), 44.6 (C-8), 61.0 (C-9), 38.3 (C-10), 200.4 (C-11), 126.8 (C-12), 170.7 (C-13), 43.1 (C-14), 25.4 (C-15), 25.3 (C-16), 30.8 (C-17), 47.7 (C-18), 40.2 (C-19), 42.4 (C-20), 29.8 (C-21), 36.4 (C-22), 26.3 (C-23), 14.8 (C-24), 14.8 (C-25), 17.1 (C-26), 21.6 (C-27), 26.8 (C-28), 26.0 (C-29), 174.8 (C-30), 104.6 (C-1′), 60.7 (C-6′), 69.6 (C-5′), 76.9 (C-4′), 76.2 (C-3′), 73.6 (C-2′), 93.6 (C-1″), 60.5 (C-6″), 76.2 (C-5″), 72.0 (C-4″), 69.2 (C-3″), 75.6 (C-2″). The calculated ESI-HRMS of 18β-GA-3,30-*O*-β-bis-Man ($C_{42}H_{66}O_{14}$) was 794.4453 g mol^{-1}. The experimental peak of m/z = 795.4525 was considered as $[M + H]^+$.

5.2.7 18β-GA-30-*O*-β-Gal (9). ^{1}H NMR (700 MHz, methanol-d_4, CD_3OD): δ 5.61 (s, 1H, H-12), 5.46 (d, J = 8.2 Hz, 1H, H-1), 3.16 (dd, J = 11.8, 4.5 Hz, 1H, H-3), 2.71 (dt, J = 13.4, 3.6 Hz, 1H, H-1a), 2.43 (s, 1H, H-9), 2.14 (td, J = 13.7, 4.6 Hz, 1H, H-16b), 0.79 (s, 3H, H-24), 0.98 (s, 3H, H-23), 1.19 (s, 3H, H-29), 0.81 (s, 3H, H-28), 1.41 (s, 3H, H-27), 1.12 (s, 6H, H-25, H-26), 1.77–1.70 (m, 2H, H-2b, H-19a), 1.64–1.58 (m, 1H, H-6b), 2.27–2.22 (m, 1H, H-18), 1.26–1.20 (m, 1H, H-15a), 1.05–0.98 (m, 2H, H-1b, H-16a), 1.89–1.84 (m, 2H, H-2b, H-19b), 1.90–1.88 (m, 1H, H-15b), 1.68–1.72 (m, 1H, H-19a), 0.75 (dd, 1H, H-5), 1.49–1.35 (m, 4H, H-6a, H-7a, H-22b, H-21a), 1.50–1.42 (m, 1H, H-22a), 2.03–2.00 (m, 1H, H-21b), 1.72–1.68 (m, 1H, H-7b), 3.89 (dd, J = 3.4, 1.1 Hz, 1H, H-6′b), 3.66 (dd, J = 9.7, 8.2 Hz, 1H, H-6′a), 3.64 (m, 1H, H-2′), 3.72 (m, 1H, H-3′), 3.53 (m, 1H, H-4′), 3.62 (m, 1H, H-5′), 1.64–1.58 (m, 1H, H-6b), 0.75 (dd, J = 12.0, 1.9 Hz, 1H, H-5), 3.89 (dd, J = 12.1, 2.1 Hz, 1H, H-2′b), 3.66 (dd, J = 12.0, 4.9 Hz, 1H, H-6′a). ^{13}C NMR (175 MHz, methanol-d_4, CD_3OD): δ 38.9 (C-1),

30.5 (C-2), 78.0 (C-3), 38.8 (C-4), 54.7 (C-5), 17.2 (C-6), 32.4 (C-7), 45.3 (C-8), 61.7 (C-9), 36.9 (C-10), 201.2 (C-11), 127.6 (C-12), 171.3 (C-13), 43.8 (C-14), 26.0 (C-15), 26.1 (C-16), 31.5 (C-17), 48.4 (C-18), 40.8 (C-19), 43.8 (C-20), 30.5 (C-21), 37.2 (C-22), 27.2 (C-23), 15.5 (C-24), 14.9 (C-25), 17.8 (C-26), 22.3 (C-27), 27.5 (C-28), 26.7 (C-29), 175.6 (C-30), 94.9 (C-1′), 61.0 (C-6′), 73.7 (C-5′), 68.6 (C-4′), 76.1 (C-3′), 69.6 (C-2′). The calculated ESI-HRMS of 18β-GA-30-*O*-β-Gal ($C_{36}H_{56}O_9$) was 632.3924 g mol^{-1}. The experimental peak of $m/z = 633.3997$ was considered as $[M + H]^+$.

5.2.8 18β-GA-30-*O*-β-2DG (10). ^{1}H NMR (700 MHz, methanol-d_4, CD_3OD): δ 5.56 (s, 1H, H-12), 4.57 (dd, $J = 9.7$ Hz, 1H, H-1′), 3.83 (dd, $J = 11.7$, 1.7 Hz, 1H, H-2′b), 3.67 (dd, $J = 11.8$, 5.5 Hz, 1H, H-6′b), 1.46–1.50 (dd, 1H, H-2′a), 2.14 (m, 1H, H-2′b), 3.52 (ddd, $J = 11.8$, 8.6, 5.0 Hz, 1H, H-3′), 3.16 (m, 1H, H-4′), 3.17 (m, 1H, H-5′), 2.69 (dt, $J = 13.5$, 3.6 Hz, 1H, H-1a), 2.44 (s, 1H, H-9), 2.13–2.15 (m, 1H, H-16b), 1.86–1.95 (m, 2H, H-21b, H-19b), 1.90–1.88 (m, 2H, H-2b, H-15b), 1.76–1.66 (m, 3H, H-2a, H-7b, H-19a), 1.63–1.57 (m, 1H, H-6b), 1.49–1.46 (m, 1H, H-22a), 1.26–1.21 (m, 1H, H-15a), 1.16 (s, 3H, H-29), 1.13 (d, 6H, H-25, H-26), 0.80 (s, 3H, H-24), 0.82 (s, 3H, H-28), 1.41 (s, 3H, H-27), 0.78 (m, 1H, H-5), 1.05–0.98 (m, 2H, H-1b, H-16a), 3.17–3.19 (m, 1H, H-3), 1.45–1.35 (m, 4H, H-6a, H-7a, H-22b, H-21a), 2.16–2.21 (m, 1H, H-18), 0.96 (s, 3H, H-23). ^{13}C NMR (175 MHz, methanol-d_4, CD_3OD): δ 38.1 (C-1), 25.4 (C-2), 88.0 (C-3), 38.4 (C-4), 54.1 (C-5), 16.4 (C-6), 31.6 (C-7), 44.6 (C-8), 61.0 (C-9), 36.0 (C-10), 200.5 (C-11), 126.7 (C-12), 170.7 (C-13), 42.8 (C-14), 25.4 (C-15), 25.2 (C-16), 30.8 (C-17), 47.8 (C-18), 40.3 (C-19), 42.5 (C-20), 29.9 (C-21), 36.9 (C-22), 26.6 (C-23), 14.8 (C-24), 14.8 (C-25), 17.1 (C-26), 21.7 (C-27), 27.0 (C-28), 26.6 (C-29), 178.2 (C-30), 101.6 (C-1′), 60.8 (C-6′), 75.8 (C-5′), 70.5 (C-4′), 71.0 (C-3′), 29.8 (C-2′). The calculated ESI-HRMS of 18β-GA-30-*O*-β-2-DG ($C_{36}H_{56}O_8$) was 616.3975 g mol^{-1}. The experimental peak of $m/z = 639.3867$ was considered as $[M + Na]^+$.

5.2.9 18β-GA-30-*O*-β-2-DGal (11). ^{1}H NMR (700 MHz, methanol-d_4): δ 5.57 (s, 1H, H-12), 4.55 (dd, $J = 9.7$ Hz, 1H, H-1′), 3.80 (dd, $J = 11.9$, 1H, H-2′b), 3.65 (dd, $J = 14$ Hz, 1H, H-6′b), 1.47, 2.13 (m, 1H, H-2′a, H-2′b), 3.49 (m, 1H, H-3′), 3.18 (m, 1H, H-4′), 3.14 (m, 1H, H-5′), 2.67 (dt, $J = 13.6$, 3.7 Hz, 1H, H-1a), 2.42 (s, 1H, H-9), 2.24–2.15 (m, 1H, H-16b), 1.84–1.93 (m, 2H, H-21b, H-19b), 1.94–1.80 (m, 2H, H-2b, H-15b), 1.78–1.67 (m, 3H, H-2a, H-7b, H-19a), 1.62–1.56 (m, 1H, H-6b), 1.50–1.45 (m, 1H, H-22a), 1.19–1.22 (m, 1H, H-15a), 1.26 (s, 3H, H-29), 1.11 (d, 6H, H-25, H-26), 0.78 (s, 3H, H-24), 0.80 (s, 3H, H-28), 1.37 (s, 3H, H-27), 0.77–0.74 (m, 1H, H-5), 1.02–0.97 (m, 2H, H-1b, H-16a), 3.16–3.15 (m, 1H, H-3), 1.46–1.35 (m, 4H, H-6a, H-7a, H-22b, H-21a), 2.21–2.18 (m, 1H, H-18), 0.94 (s, 3H, H-23). ^{13}C NMR (175 MHz, methanol-d_4, CD_3OD): δ 38.1 (C-1), 25.4 (C-2), 88.0 (C-3), 38.3 (C-4), 54.1 (C-5), 16.4 (C-6), 31.6 (C-7), 44.6 (C-8), 60.9 (C-9), 35.9 (C-10), 200.5 (C-11), 126.7 (C-12), 170.9 (C-13), 43.1 (C-14), 25.4 (C-15), 25.3 (C-16), 30.8 (C-17), 47.8 (C-18), 40.6 (C-19), 42.4 (C-20), 30.1 (C-21), 37.0 (C-22), 26.8 (C-23), 14.8 (C-24), 14.8 (C-25), 17.1 (C-26), 21.7 (C-27), 27.0 (C-28), 26.6 (C-29), 178.3 (C-30), 101.6 (C-1′), 60.8 (C-6′), 75.8 (C-5′), 70.5 (C-4′), 71.0 (C-3′), 30.1 (C-2′). The calculated ESI-HRMS of 18β-GA-30-*O*-β-2-deoxy-Gal ($C_{36}H_{56}O_8$) was 616.3975 g mol^{-1}. The experimental peak of $m/z = 639.3867$ was considered as $[M + Na]^+$.

5.3 ELISA-based binding assay of ACE2 to SARS-CoV-2 spike RBD

The receptor-binding domain (RBD) sequence of the SARS-CoV-2 spike (S) protein was subcloned from the pUC57-2019-nCoV-S plasmid (Human, Molecular Cloud) into the pET28a(+) vector for protein expression in *E. coli* BL21(DE3). The recombinant RBD protein was purified using Ni-NTA affinity chromatography, and its purity was confirmed by SDS-PAGE followed by Coomassie blue staining. Purified fractions were desalted using PD-10 columns (Cytiva), concentrated with Amicon® Ultra centrifugal filters (3 kDa MWCO), quantified, aliquoted, and stored at −80 °C until use. Human ACE2 protein was kindly provided by Dr Yu-Kuo Wang (BioSmart Co., Ltd). For the ELISA assay, MaxiSorp 96-well plates (NUNC) were coated with ACE2 protein (1 μg mL^{-1} in PBS) and incubated for 1 hour at room temperature. Wells were then washed with PBS-T (PBS containing 0.05% Tween-20) and blocked with 3% BSA for 20 minutes. Next, 20 μL of PBS containing either 10 μL of test inhibitor (TI) or 2.5% DMSO (positive control, PC) was added to each well and incubated for 1 hour. Subsequently, 20 μL of RBD protein (1 ng μL^{-1}) was added and incubated for an additional hour. After washing, a 500-fold diluted mouse anti-SARS-CoV-2 spike RBD antibody (BioSmart Co., Ltd) was added and incubated for 1 hour, followed by a 200-fold diluted HRP-conjugated goat anti-mouse IgG secondary antibody (Jackson ImmunoResearch Inc.) for another hour. Signal development was performed by adding 100 μL of TMB substrate (Merck) for 20 minutes, and the reaction was stopped with 50 μL of 2 M HCl. Absorbance was measured at 450 nm. The inhibition rate was calculated using the following formula: inhibition rate (%) = (1 − (absorbance of TI/absorbance of PC)) × 100%. All experiments were performed in triplicate, and results are expressed as mean ± standard deviation.

5.4 M^{pro} inhibitory activity assay

The inhibitory activity of 18β-GA glycosides against M^{pro} was evaluated using the "3CL Protease, MBP-tagged (SARS-CoV-2) Assay Kit" (BPS Bioscience). Briefly, purified MBP-tagged M^{pro} (50 nM) was incubated with serial dilutions of the test compounds at 37 °C for 30 minutes. A fluorogenic substrate (DABCYL–KTSAVLQSGFRKME–EDANS) was then added, and the reaction mixture was incubated for an additional hour under the same conditions. Control wells contained the same concentrations of the test compounds but without the enzyme. Protease activity was measured by monitoring the fluorescence of EDANS released upon substrate cleavage (excitation/emission: 355 nm/460 nm) using a Fluoroskan Ascent FL fluorometer. The percentage inhibition was calculated by comparing the fluorescence intensity of the test wells to that of the controls. IC_{50} values were determined using nonlinear regression analysis with GraphPad Prism 8.0.1, using 100% enzyme activity as the reference point.

5.5 Biolayer interferometry

Label-free bio-layer interferometry (BLI) assays were performed using an Octet K2 two-channel system (FortéBio) at the Center for Emergent Functional Matter Science, National Yang Ming Chiao Tung University, following standard protocols. Experiments were conducted at 30 °C with a shaking speed of 1000 rpm, using phosphate-buffered saline with 0.1% Tween-20 (PBS-T) as the running buffer.[49] Ni-NTA biosensors were prepared by first equilibrating the probes in PBS-T for 60 seconds, followed by loading with 200 μL of M^{pro}-His solution (50 μg mL^{-1}) for 120 seconds. The loaded probes were then re-equilibrated in PBS-T for an additional 60 seconds. For binding kinetics analysis, 18β-GA glycosides were serially diluted in PBS-T, and both test samples and controls were placed in separate rows of black polypropylene microplates. Each BLI cycle consisted of four steps: baseline normalization (30 seconds), association (150 seconds), dissociation (150 seconds), and regeneration (30 seconds in 10 mM glycine buffer, pH 1.7). Data were processed using FortéBio Data Analysis High Throughput 12.0. Savitzky–Golay filtering was applied to minimize high-frequency noise. Specific binding signals were determined using the "dual reference" subtraction method, which accounts for both the reference sensor and baseline drift. Kinetic parameters were calculated using a 1 : 1 binding model.

5.6 Molecular docking of 18β-GA glycosides with M^{pro}

Molecular docking of GL, 18β-GA, and their glycosides with SARS-CoV-2 M^{pro} was performed using iGEMDOCK software.[50] The chemical structures of all compounds were drawn in ChemDraw 12.0 and converted to Mol files using ChemBio3D Ultra. The X-ray crystal structure of the M^{pro}–GC376 complex (PDB ID: 6W63) was retrieved from the Protein Data Bank. Key residues within the M^{pro} active site—including His41, Cys44, Leu141, Asn142, Gly143, Ser144, Cys145, His163, His164, Met165, Glu166, Arg188, and Gln189—were identified for the docking process. Following ligand preparation and binding site definition, virtual screening and pharmacological interaction analyses were conducted. The optimal docking poses were selected based on the lowest binding free energy values. Docking results were analyzed and visualized using PyMOL2 (version 2.3.3; Schrödinger/Accelrys, San Diego, CA, USA).

Author contributions

T.-K. W.: conceptualization, supervision, writing – original draft, writing – review & editing. F.-P. C. performed the bioassay, writing – part original draft. E.-Y. L., S.-C. C. and T.-Y. H. performed enzymatic synthesis, bioassay and molecular docking studies. S.-C. H. performed compound structural analysis. All authors gave final approval for publication and agreed to be held accountable for the work performed therein.

Conflicts of interest

The authors declare that there are no conflicts of interest to declare.

Data availability

Additional datasets generated and analyzed during the current study are available from the corresponding author upon reasonable request.

All data supporting the findings of this study are available within the article and its SI. See DOI: **https://doi.org/10.1039/d5ra04664e**.

Acknowledgements

This work was financially supported by the Ministry of Science and Technology, Taiwan (grant no. MOST 107-2113-M-009-009, MOST 110-2113-M-A49-017, and MOST 112-2113-M-A49-008), the Center for Emergent Functional Matter Science, and the Center for Intelligent Drug Systems and Smart Bio-devices (IDS^2B) of National Yang Ming Chiao Tung University from The Featured Areas Research Center Program within the framework of the Higher Education Sprout Project by the Ministry of Education (MOE) in Taiwan.

References

1 World Health Organization (WHO), 2025, **https://www.who.int/emergencies/disease-outbreak-news/item/2025-DON572**.
2 S. D. Gupta, *J. Health Manage.*, 2025, **27**, 307.
3 S. Moreno, B. Alcázar, C. Dueñas, J. González Del Castillo, J. Olalla and A. Antela, *Drug Des., Dev. Ther.*, 2022, **25**, 827–841.
4 L. D. Saravolatz, S. Depcinski and M. Sharma, *Clin. Infect. Dis.*, 2023, **76**, 165–171.
5 Z. Zeng, C. Liao and L. Yu, *Chin. Chem. Lett.*, 2024, **35**, 109349.
6 H. Liu, S. Chen, M. Liu, H. Nie and H. Lu, *Aging Dis.*, 2020, **11**, 668–678.
7 Y. Xie, B. Bowe, G. Maddukuri and Z. Al-Aly, *BMJ [Br. Med. J.]*, 2020, **371**, m4677.
8 R. E. Thomas, *Geriatrics*, 2021, **6**, 48.
9 Q. S. Du, S. Q. Wang, Y. Zhu, D. Q. Wei, H. Guo, S. Sirois and K. C. Chou, *Peptides*, 2004, **25**, 1857–1864.
10 R. Jain and S. Mujwar, *Struct. Chem.*, 2020, **36**, 2487–2499.
11 H. M. Mengist, T. Dilnessa and T. Jin, *Front. Chem.*, 2021, **9**, 622898.
12 M. Shinada, M. Azuma, H. Kawai, K. Sazaki, I. Yoshida, T. Yoshida, T. Suzutani and T. Sakuma, *Proc. Soc. Exp. Biol. Med.*, 1986, **181**, 205–210.
13 J. M. Crance, F. Lévêque, E. Biziagos, H. van Cuyck-Gandré, A. Jouan and R. Deloince, *Antiviral Res.*, 1994, **23**, 63–76.
14 S. Harada, T. Maekawa, E. Haneda, Y. Morikawa, N. Nagata and K. Ohtsuki, *Biol. Pharm. Bull.*, 1998, **21**, 1282–1285.

15 J. Cinatl, B. Morgenstern, G. Bauer, P. Chandra, H. Rabenau and H. W. Doerr, *Lancet*, 2003, **361**, 2045–2046.
16 L. A. Baltina, R. M. Kondratenko, L. A. J. Baltina, O. A. Plyasunova, A. G. Pokrovskii and G. A. Tolstikov, *Pharm. Chem. J.*, 2009, **43**, 539–548.
17 U. A. Ashfaq, M. S. Masoud, Z. Nawaz and S. Riazuddin, *J. Transl. Med.*, 2011, **9**, 112.
18 Y. Kondo and F. Takano, *Biol. Pharm. Bull.*, 1994, **17**, 759–761.
19 N. K. Bordbar, M. H. Karimi and Z. Amirghofran, *Cell. Immunol.*, 2012, **280**, 44–49.
20 C. Y. Wang, T. C. Kao, W. H. Lo and G. C. Yen, *J. Agric. Food Chem.*, 2011, **59**, 7726–7733.
21 I. Fatima, A. Sahar, A. Tariq, T. Naz and M. Usman, *J. Nutr. Metab.*, 2024, **2024**, 9988167.
22 J. Li, D. Xu, L. Wang, M. Zhang, G. Zhang, E. Li and S. He, *Molecules*, 2021, **26**, 6090.
23 L. van de Sand, M. Bormann, M. Alt, L. Schipper, C. S. Heilingloh, E. Steinmann, D. Todt, U. Dittmer, C. Elsner, O. Witzke and A. Krawczyk, *Viruses*, 2021, **13**, 609.
24 S. Yu, Y. Zhu, J. Xu, G. Yao, P. Zhang, M. Wang, Y. Zhao, G. Lin, H. Chen, L. Chen and J. Zhang, *Phytomedicine*, 2021, **85**, 153364.
25 C. Bailly and G. Vergoten, *Pharmacol. Ther.*, 2020, **214**, 107618.
26 H. Li, Y. Hu, H. Tang, S. Li, H. Ding, S. Zhai and R. Zhao, *Am. J. Chin. Med.*, 2020, **48**, 1539–1552.
27 S. Mahdian, A. Ebrahim-Habibi and M. Zarrabi, *J. Diabetes Metab. Disord.*, 2020, **19**, 691–699.
28 S. Banerjee, S. K. Baidya, N. Adhikari, B. Ghosh and T. Jha, *J. Mol. Struct.*, 2023, **1275**, 134642.
29 T. Moses, K. K. Papadopoulou and A. Osbourn, *Crit. Rev. Biochem. Mol. Biol.*, 2014, **49**, 439–462.
30 R. Bansal and A. Suryan, *ACS Bio Med Chem Au*, 2022, **2**, 340–369.
31 H. F. Liu, S. C. Chou, S. C. Huang, T. Y. Huang, P. Y. Hsiao, F. P. Chou and T. K. Wu, *Chem. Biol. Drug Des.*, 2024, **104**, e14624.
32 F. P. Chou, C. T. Tsai, Y. S. Chiou, Y. J. Chen, M. E. Li, T. W. Guo, J. W. Lyu, S. H. Chou and T. K. Wu, *Chem. Biol. Drug Des.*, 2017, **89**, 61–66.
33 F. P. Chou, W. C. Hsu, S. C. Huang, C. Y. Chang, Y. S. Chiou, C. T. Tsai, J. W. Lyu, W. T. Chen and T. K. Wu, *Chem. Commun.*, 2020, **56**, 1733–1736.
34 A. H. Lebrun, C. Wunder, J. Hildebrand, Y. Churin, U. Zähringer, B. Lindner, T. F. Meyer, E. Heinz and D. Warnecke, *J. Biol. Chem.*, 2006, **281**, 27765–27772.
35 M. Nishimoto and M. Kitaoka, *Appl. Environ. Microbiol.*, 2007, **73**, 6444–6449.
36 M. M. Muthana, J. Qu, Y. Li, L. Zhang, H. Yu, L. Ding, H. Malekan and X. Chen, *Chem. Commun.*, 2012, **48**, 2728–2730.
37 L. Dai, J. Li, P. Yao, Y. Zhu, Y. Men, Y. Zeng, J. Yang and Y. Sun, *J. Biotechnol.*, 2017, **248**, 69–76.
38 C. A. Lipinski, F. Lombardo, B. W. Dominy and P. J. Feeney, *Adv. Drug Delivery Rev.*, 2001, **46**, 3–26.
39 L. Fu, F. Ye, Y. Feng, F. Yu, Q. Wang, *et al.*, *Nat. Commun.*, 2020, **11**, 4417.
40 B. C. Doak, B. Over, F. Giordanetto and J. Kihlberg, *Chem. Biol.*, 2014, **21**, 1115–1142.
41 B. C. Doak and J. Kihlberg, *Expert Opin. Drug Discovery*, 2017, **12**, 115–119.
42 E. C. de Oliveira, K. Santana, L. Josino, E. Lima, A. H. Lima and J. C. de Souza de Sales, *Sci. Rep.*, 2021, **11**, 7628.
43 J. Kügler, S. Schmelz, J. Gentzsch, S. Haid, E. Pollmann, J. van den Heuvel, R. Franke, T. Pietschmann, D. W. Heinz and J. Collins, *J. Biol. Chem.*, 2012, **287**, 39224–39232.
44 W. Vuong, M. B. Khan, C. Fischer, E. Arutyunova and T. Lamer, *Nat. Commun.*, 2020, **11**, 4282.
45 N. Higashi-Kuwata, H. Bulut, H. Hayashi, K. Tsuji, H. Ogata-Aoki, M. Kiso, N. Takamune, N. Kishimoto, S.-I. Hattori, T. Ishii, *et al.*, *PNAS Nexus*, 2025, **4**, 578.
46 W. C. Chiou, M. S. Hsu, Y. T. Chen, J. M. Yang, Y. G. Tsay, H. C. Huang and C. Huang, *J. Enzyme Inhib. Med. Chem.*, 2021, **36**, 147–153.
47 M. von Itzstein, W. Y. Wu, G. B. Kok, M. S. Pegg, J. C. Dyason, B. Jin, T. Van Phan, M. L. Smythe, H. F. White, S. W. Oliver, *et al.*, *Nature*, 1993, **363**, 418–423.
48 M. Iikura, T. Furihata, M. Mizuguchi, M. Nagai, M. Ikeda, N. Kato, A. Tsubota and K. Chiba, *Antimicrob. Agents Chemother.*, 2012, **56**, 1407–1413.
49 H. N. H. Giang, F. P. Chou, C. Y. Chen, S. C. Chou, S. C. Huang, T. Wu, B. T. B. Hue, H. C. Lin and T. K. Wu, *Viruses*, 2023, **15**, 287.
50 K. C. Hsu, Y. F. Chen, S. R. Lin and J. M. Yang, *BMC Bioinf.*, 2011, **12**, S33.